MIT Libraries | DSpace@MIT

MIT Open Access Articles

Synthetic Lateral Metal-Semiconductor Heterostructures of Transition Metal Disulfides

The MIT Faculty has made this article openly available. ***Please share*** how this access benefits you. Your story matters.

Citation: Leong, Wei Sun et al. "Synthetic Lateral Metal-Semiconductor Heterostructures of Transition Metal Disulfides." Journal of the American Chemical Society 140, 39 (September 2018): 12354-12358 © 2018 American Chemical Society

As Published: http://dx.doi.org/10.1021/jacs.8b07806

Publisher: American Chemical Society (ACS)

Persistent URL: https://hdl.handle.net/1721.1/121574

Version: Author's final manuscript: final author's manuscript post peer review, without publisher's formatting or copy editing

Terms of Use: Article is made available in accordance with the publisher's policy and may be subject to US copyright law. Please refer to the publisher's site for terms of use.

Massachusetts Institute of Technology

JACS
JOURNAL OF THE AMERICAN CHEMICAL SOCIETY
Cite This: J. Am. Chem. Soc. XXXX, XXX, XXX−XXX
Communication
pubs.acs.org/JACS

Synthetic Lateral Metal-Semiconductor Heterostructures of Transition Metal Disulfides

Wei Sun Leong,[†,+] Qingqing Ji,*[,‡,+] Nannan Mao,[†,+] Yimo Han,[§] Haozhe Wang,[†] Aaron J. Goodman,[∥] Antoine Vignon,[‡] Cong Su,[‡,⊥] Yunfan Guo,[‡] Pin-Chun Shen,[†] Zhenfei Gao,[‡,#] David A. Muller,[§,¶] William A. Tisdale,[⊗] and Jing Kong*[,†,‡]

[†]Department of Electrical Engineering and Computer Science, Massachusetts Institute of Technology, Cambridge, Massachusetts 02139, United States

[‡]Research Laboratory of Electronics, Massachusetts Institute of Technology, Cambridge, Massachusetts 02139, United States

[§]School of Applied and Engineering Physics, Cornell University, Ithaca, New York 14853, United States

[∥]Department of Chemistry, Massachusetts Institute of Technology, Cambridge, Massachusetts 02139, United States

[⊥]Department of Nuclear Science and Engineering and Department of Materials Science and Engineering, Massachusetts Institute of Technology, Cambridge, Massachusetts 02139, United States

[#]State Key Laboratory of Heavy Oil Processing, China University of Petroleum, Beijing 102200, People's Republic of China

[¶]Kavli Institute at Cornell for Nanoscale Science, Ithaca, New York 14853, United States

[⊗]Department of Chemical Engineering, Massachusetts Institute of Technology, Cambridge, Massachusetts 02139, United States

Supporting Information

ABSTRACT: Lateral heterostructures with planar integrity form the basis of two-dimensional (2D) electronics and optoelectronics. Here we report that, through a two-step chemical vapor deposition (CVD) process, high-quality lateral heterostructures can be constructed between metallic and semiconducting transition metal disulfide (TMD) layers. Instead of edge epitaxy, polycrystalline monolayer MoS_2 in such junctions was revealed to nucleate from the vertices of multilayered VS_2 crystals, creating one-dimensional junctions with ultralow contact resistance (0.5 kΩ·μm). This lateral contact contributes to 6-fold improved field-effect mobility for monolayer MoS_2, compared to the conventional on-top nickel contacts. The all-CVD strategy presented here hence opens up a new avenue for all-2D-based synthetic electronics.

Functional heterostructures are indispensable building blocks for modern electronics and optoelectronics.[1] With recent advancement in flexible and deformable electronics,[2,3] an emerging requirement arises in thinning down the host materials in these heterostructures to fulfill such targets. Two-dimensional (2D) transition metal dichalcogenides[4,5] (TMDs), as a group of inorganic van der Waals (vdW) materials, can be potential candidates for building such ultrathin heterostructures. Diverse TMD layers, as well as other 2D materials, have been isolated and combined into heterostacks, termed vdW heterostructures,[6] to serve as tunneling transistors,[7] light-emitting diodes,[8] photodetectors,[9] and photovoltaic cells.[10] Moreover, the lattice-structure similarity of all TMDs, combined with their tunable electronic properties, has enabled them to epitaxially stitch and integrate in the 2D plane,[11−14] forming lateral heterostructures of ultimate thinness and comparable functionalities to their vdW heterostructure analogues.

While significant progresses have been made recently in the chemical vapor deposition (CVD) of edge-epitaxy lateral TMD heterostructures and superlattices,[15−17] most of the prior works focused on semiconductor-semiconductor junctions that have diode-like rectifying properties. It remains an open question whether such edge-epitaxy schemes can be extrapolated to other types of lateral heterostructures, one of which, being a key component in modern electronics and optoelectronics, is the metal-semiconductor TMD junctions. Although fundamental understandings on such one-dimensional (1D) "Schottky" junctions are still limited, they have been predicted to have unique depletion profiles[18] that contributes to ultralow-resistance contacts,[19,20] a property greatly desired for high-performance 2D electronics.[21] However, CVD growth of lateral metal-semiconductor TMD heterostructures is still challenging because of the chemical instability of metallic TMDs, and the unknown surface/edge energetics of both, leading to either in-phase alloying,[22] vertical stacking, or coplanar stitching.[11] It is hence imperative to uncover, understand, and finally control their growth behaviors to achieve desirable configurations of metal-semiconductor TMD heterostructures.

Here we take VS_2 and MoS_2, the representative metallic and semiconducting TMDs, respectively, as an example to demonstrate that CVD techniques can be used to synthesize and stitch the two complementary materials to form lateral heterostructures. Interestingly, polycrystalline monolayer MoS_2 in such junctions was revealed to nucleate from the vertices of multilayer VS_2 crystals, rather than epitaxially grow from their

Received: July 31, 2018
Published: September 20, 2018

Downloaded via MASSACHUSETTS INST OF TECHNOLOGY on September 24, 2018 at 14:07:20 (UTC).
See https://pubs.acs.org/sharingguidelines for options on how to legitimately share published articles.

ACS Publications © XXXX American Chemical Society

DOI: 10.1021/jacs.8b07806
J. Am. Chem. Soc. XXXX, XXX, XXX−XXX

edges. The obtained lateral VS_2−MoS_2 heterostructures exhibit remarkable contact properties with Schottky barrier height as small as ∼30 meV, contributing to a 6-fold improved field-effect mobility for monolayer MoS_2, compared to conventional on-top nickel contacts. This opens up an avenue for all-TMD-based synthetic 2D electronics.

Figure 1a,b shows the atomic models of VS_2 and MoS_2 that crystallize in 1T and 2H phases, respectively, whose electronic structures are schematically illustrated in Figure 1c,d. Although VS_2 is a metal and MoS_2 is a semiconductor by nature, they have similar sulfur−metal−sulfur sandwiched layers and close in-plane lattice periodicities of ∼0.32 nm. This offers the possibility that the two TMD materials can be parallelly stitched with minimal strain at the 1D interface. In our experiment, the construction of such lateral junctions involves two sequential steps: synthesis of VS_2 nanosheets and growth of MoS_2 nanosheets. This two-step CVD process offers precise control for an abrupt transition from presynthesized VS_2 to the secondarily grown MoS_2 layers. Figure 1e schematically shows the second-step MoS_2 growth on a SiO_2/Si substrate with pregrown VS_2 nanosheets. Marked by the blue and red arrows are the two possible growth mechanisms mediated either by the edge or the surface of VS_2, which will be discussed later.

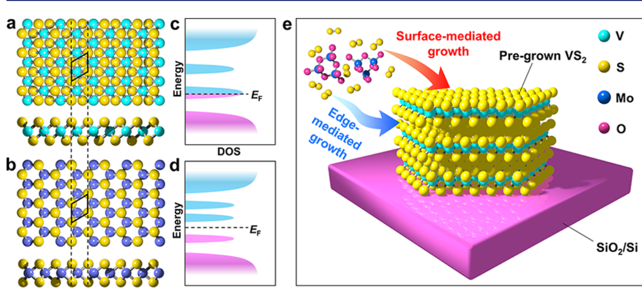

Figure 1. Construction of MoS_2−VS_2 heterostructures. (a, b) Atomic models of 1T-VS_2 and 2H-MoS_2, respectively. The rhombuses mark the unit cells of the two. (c, d) Schematic density of states of VS_2 and MoS_2 near their Fermi levels. The filled and unfilled states are colored in red and blue, respectively. (e) Schematic illustration of the second-step MoS_2 growth mediated either by the edge or the surface of the pregrown VS_2 nanosheets.

The CVD of individual VS_2 and MoS_2 nanosheets was performed at first, whose methodologies are similar to our previous reports[23,24] (see Figure S1 and S2 for more details). As shown in Figure 2a, the VS_2 nanosheets manifest unique half-hexagonal shapes and uniform optical contrast, which can be associated with homogeneous thicknesses of 5−7 nm (Figure S3c), as measured by atomic force microscopy (AFM). We note that although the VS_2 prepared by such CVD methods is slightly nonstoichiometric, its 1T-phase framework persists along with the high electrical conductivity, hence exerting no influence on the construction of metal-semiconductor heterostructures with MoS_2. The morphology of MoS_2 nanosheets, on the other hand, is different from that of VS_2 in that the grain structures are more complicated with triangular and polygonal outlines (Figure 2b), and the sheet thickness can be down to monolayer (Figure S3f). Under scanning electron microscopy (SEM), the VS_2 flakes show brighter contrast than the MoS_2 flakes (Figure 2d,e), which is consistent with the fact that VS_2 is metallic whereas MoS_2 is semiconducting.

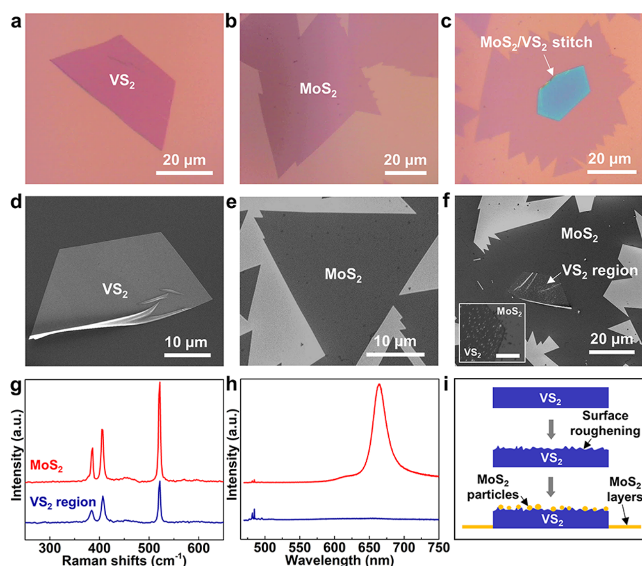

Figure 2. CVD-derived 2D nanosheets of VS_2, MoS_2 and their heterostructures. (a−c) Optical images of the three. (d−f) Corresponding SEM images. Inset in panel f is the zoomed-in SEM image of a lateral VS_2−MoS_2 interface (scale bar 2 μm). (g, h) Raman and PL spectra on the central VS_2 region and the surrounding MoS_2 region (blue and red curves, respectively) for the MoS_2−VS_2 heterostructures. (i) Schematic illustration of MoS_2 growth on presynthesized multilayered VS_2.

With the optimized growth of individual VS_2 and MoS_2 nanosheets, their 2D heterostructures can be readily achieved by the two-step growth process. Figure 2c shows a typical optical image of the lateral MoS_2−VS_2 heterostructure. As can be seen, MoS_2 tends to grow outward from and encompass the pregrown VS_2 nanosheet, tuning the optical contrast of VS_2 from purple to blue (Figure 2c). Sharp optical contrast is observed between VS_2 and MoS_2 along the edges of VS_2, indicating that the MoS_2 grown in the second step laterally stitches to VS_2. The parallel stitching was further evidenced under higher spatial resolution by AFM (Figure S3), SEM (Figure 2f) and transmission electron microscopy (Figure S4) studies, together with more detailed discussions in the Supporting Information.

One significant feature for the VS_2 region after MoS_2 growth is the higher surface roughness (2.3 nm) compared to its as-grown state (0.15 nm) (Figure S3g). This can be directly observed in the SEM image of the lateral heterostructure (inset in Figure 2f), showing nanosized dots on VS_2 surface that indicates formation of nanoparticles. Further Raman and photoluminescence characterizations (Figure 2g,h) reveal signals of multilayered, particulate MoS_2 on the VS_2 region. Such granular rather than layered growth of MoS_2 on VS_2 surface can be attributed to the surface roughening of VS_2 under a high-temperature oxidative atmosphere (Figure S3d). Nevertheless, the sharp switching of MoS_2 morphologies divided by the VS_2 edges suggests an effective decoupling of the MoS_2 growth on and surrounding the VS_2 flakes (Figure 2i).

The commonly observed star shapes of MoS_2 surrounding VS_2 flakes is a strong indication that the MoS_2 rims are not single crystalline (Figure S5). This is in contradiction with an edge epitaxy behavior[13] where the surrounding MoS_2 should have had its lattice orientationally aligned with the internal VS_2 crystals. Second harmonic generation (SHG) imaging was then

DOI: 10.1021/jacs.8b07806
J. Am. Chem. Soc. XXXX, XXX, XXX−XXX

employed to uncover the domain orientations and the grain boundaries (GBs) within MoS_2. Figure 3a is the optical image of a lateral MoS_2−VS_2 heterostructure being characterized. Corresponding SHG images of the total intensity, as well as the y- and x-polarized components are presented in Figure 3b−d, respectively. The orientation of a specific MoS_2 domain can be calculated using $\theta = \frac{1}{3}\arctan\sqrt{I_x/I_y}$, where the orientation θ is defined as the angle between incident polarization (along the x axis) and the nearest armchair axis of the domain,[25] and $I_{x(y)}$ is the $x(y)$-polarized SHG intensity.

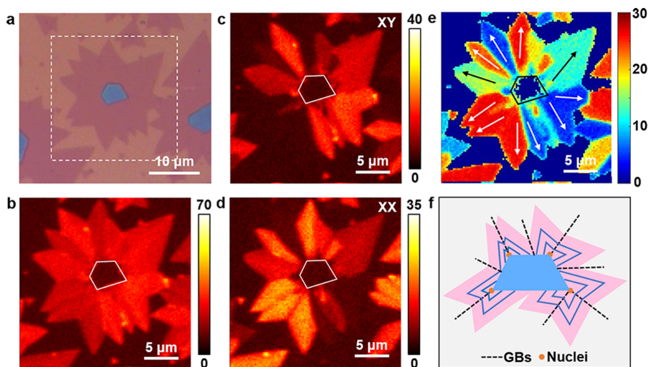

Figure 3. SHG imaging of the lateral MoS_2−VS_2 heterostructures. (a) Optical image of a MoS_2−VS_2 junction. (b) Total SHG intensity mapping of the MoS_2−VS_2 junction. Incident polarization was set along the x axis. (c, d) Intensity mapping of the y- and x-polarized SHG emissions, respectively, from the heterostructure. (e) Orientation distribution of surrounding MoS_2 domains. Arrows indicate armchair orientations of corresponding domains. (f) Schematic illustration of a possible stitching growth mechanism of MoS_2 initiated from the vertices of a presynthesized VS_2 flake. Blue lines mark the intermediate growth fronts.

As such, the orientation distribution of surrounding MoS_2 domains was calculated and plotted in Figure 3e, explicitly revealing the polycrystalline nature. Arrows were superposed on the image to mark out the armchair directions of MoS_2, which surprisingly point from the nearest VS_2 vertices to the outmost vertices of the corresponding MoS_2 domains. The GBs, on the other hand, were found to originate from VS_2 vertices and orientationally bisect neighboring two arrows. We note that such grain structures are commonly observed in all the lateral MoS_2−VS_2 heterostructures (Figure S6), confirming a universal growth mechanism. While the mirror-symmetric GBs can be explained by kinetic models that consider the interplay between growth front and GB propagation,[26,27] the above SHG results suggest that the star-shaped MoS_2 in our case is due to multicenter nucleation from the VS_2 vertices, instead of epitaxy from VS_2 edges. For this, a schematic model is proposed in Figure 3f illustrating the nonepitaxial growth of MoS_2 surrounding VS_2, in consistency with all the observed grain structure characteristics.

Although the VS_2 flakes become rougher after MoS_2 growth, their resistances were found to show negligible changes compared to as-grown ones (Figure 4b and Table S1). This allows us to exploit them as the lateral contacts to monolayer MoS_2 for field-effect transistor (FET) applications. Figure 4c compares the output characteristics of MoS_2 devices with VS_2 and Ni contacts, both of which exhibit linear I_{DS}−V_{DS} relationships, indicating their Ohmic-like contact behavior. Remarkably, with the same V_G and V_{DS} applied, the I_{DS} for the VS_2-contacted device are consistently 6 times higher than that of the Ni-contacted counterpart. In terms of their transfer characteristics (Figure 4d), the two devices show nearly identical threshold voltages (−35 V), subthreshold swings (2.5 V dec^{-1}), and on/off ratios (10^6). This indicates that the two MoS_2 channels are essentially the same in the doping level and the density of gap states, and the improved on-state currents for the VS_2-contacted device can be exclusively attributed to the decreased contact resistance. As expected, the field-effect mobility (μ_{FE}) for the VS_2-contacted device reaches as high as 35 $cm^2\ V^{-1}\ s^{-1}$, at least six time higher than that of the Ni-contacted counterpart (5.5 $cm^2\ V^{-1}\ s^{-1}$).

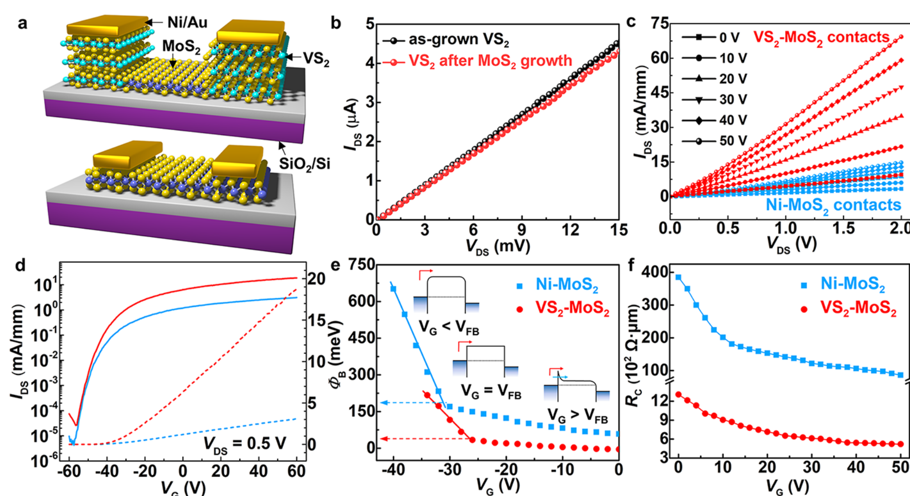

Figure 4. Electrical characterizations of the lateral VS_2−MoS_2 heterostructures. (a) Schematics showing monolayer MoS_2 field-effect transistors (FETs) with the lateral VS_2 contacts (upper) and vertical Ni contacts (lower). (b) I_{DS}−V_{DS} characteristics of a typical VS_2 electrode before and after MoS_2 growth. (c) I_{DS}−V_{DS} characteristics of MoS_2 devices with VS_2 and Ni contacts, with V_G ranging from 0 to 50 V. (d) I_{DS}−V_G characteristics of both types of devices in linear (dashed) and logarithmic scales (solid), respectively. (e) Schottky barrier heights (Φ_B) of VS_2- and Ni-contacted MoS_2 devices, as a function of V_G. Dashed arrows indicate flat-band Φ_B. (f) Contact resistances for MoS_2 FETs with VS_2 and Ni contacts, at different V_G.

DOI: 10.1021/jacs.8b07806
J. Am. Chem. Soc. XXXX, XXX, XXX−XXX

Temperature-dependent electrical measurements (Figure S7) were then performed to extract the Schottky barrier heights (Φ_B) of both types of MoS_2 devices. Figure 4e compares their extracted Φ_B at different V_G. Whereas the flat-band Φ_B for conventional Ni−MoS_2 contacts is ~163 meV, similar to previously reported values,[28,29] the Φ_B for our lateral VS_2−MoS_2 contacts is as small as 30 meV, which is one of the lowest barrier heights that outperforms many low-work-function metal contacts.[28] Furthermore, contact resistances (R_C) of the two typical devices were extracted from four-probe measurements (Figure S8) and plotted in Figure 4f. The R_C for lateral VS_2−MoS_2 contacts was found to be 520 Ω·μm at V_G = 50 V, which is more than ten times smaller than that of Ni−MoS_2 contacts (8640 Ω·μm). Note that on-top metal contacts generally result in R_C of several kΩ·μm.[30,31] Evidently, the lateral contact scheme based on our VS_2−MoS_2 heterostructures dramatically lowers the contact resistance and effectively boosts the performance of MoS_2 FETs, close to that with phase-engineered 1T-MoS_2[19] and 1T′-$MoTe_2$[20] contacts.

In summary, we have successfully demonstrated the growth of lateral MoS_2−VS_2 heterostructures using a two-step CVD strategy. We found that the latter growth of MoS_2 surrounding the presynthesized VS_2 flakes was mediated by the VS_2 vertices rather than the edges, leading to polycrystalline MoS_2 rims that laterally stitch the VS_2 flakes. Such coplanar VS_2 contacts were proven by electrical measurements to offer a low-barrier 1D interface to the semiconducting MoS_2 monolayer, improving the field-effect mobility and contact resistance by nearly 1 order of magnitude, as compared to the conventional on-top metal contacts. We postulate that the all-CVD strategy presented here will open up an avenue for TMD-based synthetic 2D electronics in a straightforward, scalable and cost-effective way.

■ ASSOCIATED CONTENT

Supporting Information

The Supporting Information is available free of charge on the ACS Publications website at DOI: 10.1021/jacs.8b07806.

Experimental details and supporting figures (PDF)

■ AUTHOR INFORMATION

Corresponding Authors

*jingkong@mit.edu

*qji@mit.edu

ORCID

Wei Sun Leong: 0000-0001-8131-2468

Qingqing Ji: 0000-0001-5526-3746

Yimo Han: 0000-0003-0563-4611

William A. Tisdale: 0000-0002-6615-5342

Jing Kong: 0000-0003-0551-1208

Author Contributions

[+]W.S.L., Q.J. and N.M. contributed equally to this work.

Notes

The authors declare no competing financial interest.

■ ACKNOWLEDGMENTS

W.S.L. acknowledges the support from AFOSR FATE MURI, Grant No. FA9550-15-1-0514. Q.J. acknowledges support by the STC Center for Integrated Quantum Materials, NSF Grant No. DMR-1231319. N.M. acknowledges support from NSF Grant 2DARE (EFRI-1542815) and DMR-1507806. H.W. acknowledges the support from NSF DMR/ECCS-1509197. P.C.S. acknowledges support from the Center for Energy Efficient Electronics Science (NSF Award 0939514). C.S. acknowledges support from U.S. Army Research Office through the MIT Institute for Soldier Nanotechnologies (Grant No. 023674). Y.H. and D.A.M. acknowledge Cornell Center for Materials Research with funding from the NSF MRSEC program (DMR-1719875). W.A.T. acknowledges support from the U.S. Department of Energy, Office of Science, through grant DE-SC0010538. Work was partially performed at Center for Nanoscale Systems, Harvard University.

■ REFERENCES

(1) Brennan, K. F.; Brown, A. S. *Theory of Modern Electronic Semiconductor Devices*; John Wiley & Sons, Inc., 2003.

(2) Sun, Y.; Rogers, J. A. *Adv. Mater.* **2007**, *19* (15), 1897−1916.

(3) Dimitrakopoulos, C. D.; Malenfant, P. R. L. *Adv. Mater.* **2002**, *14* (2), 99−117.

(4) Wang, Q. H.; Kalantar-Zadeh, K.; Kis, A.; Coleman, J. N.; Strano, M. S. *Nat. Nanotechnol.* **2012**, *7*, 699−712.

(5) Chhowalla, M.; Shin, H. S.; Eda, G.; Li, L.-J.; Loh, K. P.; Zhang, H. *Nat. Chem.* **2013**, *5*, 263−275.

(6) Geim, A. K.; Grigorieva, I. V. *Nature* **2013**, *499*, 419−425.

(7) Sarkar, D.; Xie, X.; Liu, W.; Cao, W.; Kang, J.; Gong, Y.; Kraemer, S.; Ajayan, P. M.; Banerjee, K. *Nature* **2015**, *526*, 91−95.

(8) Withers, F.; Del Pozo-Zamudio, O.; Mishchenko, A.; Rooney, A. P.; Gholinia, A.; Watanabe, K.; Taniguchi, T.; Haigh, S. J.; Geim, A. K.; Tartakovskii, A. I.; Novoselov, K. S. *Nat. Mater.* **2015**, *14*, 301−306.

(9) Massicotte, M.; Schmidt, P.; Vialla, F.; Schädler, K. G.; Reserbat-Plantey, A.; Watanabe, K.; Taniguchi, T.; Tielrooij, K. J.; Koppens, F. H. L. *Nat. Nanotechnol.* **2016**, *11*, 42−46.

(10) Lee, C.-H.; Lee, G.-H.; van der Zande, A. M.; Chen, W.; Li, Y.; Han, M.; Cui, X.; Arefe, G.; Nuckolls, C.; Heinz, T. F.; Guo, J.; Hone, J.; Kim, P. *Nat. Nanotechnol.* **2014**, *9*, 676−681.

(11) Gong, Y.; Lin, J.; Wang, X.; Shi, G.; Lei, S.; Lin, Z.; Zou, X.; Ye, G.; Vajtai, R.; Yakobson, B. I.; Terrones, H.; Terrones, M.; Tay, Beng K.; Lou, J.; Pantelides, S. T.; Liu, Z.; Zhou, W.; Ajayan, P. M. *Nat. Mater.* **2014**, *13*, 1135−1142.

(12) Duan, X.; Wang, C.; Shaw, J. C.; Cheng, R.; Chen, Y.; Li, H.; Wu, X.; Tang, Y.; Zhang, Q.; Pan, A.; Jiang, J.; Yu, R.; Huang, Y.; Duan, X. *Nat. Nanotechnol.* **2014**, *9*, 1024−1030.

(13) Li, M.-Y.; Shi, Y.; Cheng, C.-C.; Lu, L.-S.; Lin, Y.-C.; Tang, H.-L.; Tsai, M.-L.; Chu, C.-W.; Wei, K.-H.; He, J.-H.; Chang, W.-H.; Suenaga, K.; Li, L.-J. *Science* **2015**, *349* (6247), 524−528.

(14) Han, Y.; Li, M.-Y.; Jung, G.-S.; Marsalis, M. A.; Qin, Z.; Buehler, M. J.; Li, L.-J.; Muller, D. A. *Nat. Mater.* **2018**, *17*, 129−133.

(15) Zhang, Z.; Chen, P.; Duan, X.; Zang, K.; Luo, J.; Duan, X. *Science* **2017**, *357* (6353), 788−792.

(16) Xie, S.; Tu, L.; Han, Y.; Huang, L.; Kang, K.; Lao, K. U.; Poddar, P.; Park, C.; Muller, D. A.; DiStasio, R. A.; Park, J. *Science* **2018**, *359* (6380), 1131−1136.

(17) Sahoo, P. K.; Memaran, S.; Xin, Y.; Balicas, L.; Gutiérrez, H. R. *Nature* **2018**, *553*, 63−67.

(18) Yu, H.; Kutana, A.; Yakobson, B. I. *Nano Lett.* **2016**, *16* (8), 5032−5036.

(19) Kappera, R.; Voiry, D.; Yalcin, S. E.; Branch, B.; Gupta, G.; Mohite, A. D.; Chhowalla, M. *Nat. Mater.* **2014**, *13*, 1128−1134.

(20) Cho, S.; Kim, S.; Kim, J. H.; Zhao, J.; Seok, J.; Keum, D. H.; Baik, J.; Choe, D.-H.; Chang, K. J.; Suenaga, K.; Kim, S. W.; Lee, Y. H.; Yang, H. *Science* **2015**, *349* (6248), 625−628.

(21) Allain, A.; Kang, J.; Banerjee, K.; Kis, A. *Nat. Mater.* **2015**, *14*, 1195−1205.

(22) Komsa, H.-P.; Krasheninnikov, A. V. *J. Phys. Chem. Lett.* **2012**, *3* (23), 3652−3656.

(23) Ji, Q.; Li, C.; Wang, J.; Niu, J.; Gong, Y.; Zhang, Z.; Fang, Q.; Zhang, Y.; Shi, J.; Liao, L.; Wu, X.; Gu, L.; Liu, Z.; Zhang, Y. *Nano Lett.* **2017**, *17* (8), 4908−4916.
(24) Ling, X.; Lee, Y.-H.; Lin, Y.; Fang, W.; Yu, L.; Dresselhaus, M. S.; Kong, J. *Nano Lett.* **2014**, *14* (2), 464−472.
(25) Kumar, N.; Najmaei, S.; Cui, Q.; Ceballos, F.; Ajayan, P. M.; Lou, J.; Zhao, H. *Phys. Rev. B: Condens. Matter Mater. Phys.* **2013**, *87* (16), 161403.
(26) Zhang, Y.; Zhang, Y.; Ji, Q.; Ju, J.; Yuan, H.; Shi, J.; Gao, T.; Ma, D.; Liu, M.; Chen, Y.; Song, X.; Hwang, H. Y.; Cui, Y.; Liu, Z. *ACS Nano* **2013**, *7* (10), 8963−8971.
(27) Cheng, J.; Jiang, T.; Ji, Q.; Zhang, Y.; Li, Z.; Shan, Y.; Zhang, Y.; Gong, X.; Liu, W.; Wu, S. *Adv. Mater.* **2015**, *27* (27), 4069−4074.
(28) Das, S.; Chen, H.-Y.; Penumatcha, A. V.; Appenzeller, J. *Nano Lett.* **2013**, *13* (1), 100−105.
(29) Wang, J.; Yao, Q.; Huang, C. W.; Zou, X.; Liao, L.; Chen, S.; Fan, Z.; Zhang, K.; Wu, W.; Xiao, X.; Jiang, C.; Wu, W. W. *Adv. Mater.* **2016**, *28* (37), 8302−8308.
(30) English, C. D.; Shine, G.; Dorgan, V. E.; Saraswat, K. C.; Pop, E. *Nano Lett.* **2016**, *16* (6), 3824−3830.
(31) Leong, W. S.; Luo, X.; Li, Y.; Khoo, K. H.; Quek, S. Y.; Thong, J. T. L. *ACS Nano* **2015**, *9* (1), 869−877.

DOI: 10.1021/jacs.8b07806
J. Am. Chem. Soc. XXXX, XXX, XXX−XXX

View publication stats